LETTER

Scale-by-scale energy transfers and fluxes in compressible turbulence

A Letters Journal Exploring the Frontiers of Physics

June 2026

EPL, **154** (2026) 53001
doi: 10.1209/0295-5075/ae65d9

www.epljournal.org

Scale-by-scale energy transfers and fluxes in compressible turbulence

Dhananjay Singh[1], Harshit Tiwari[1(a)], Lekha Sharma[1] and Mahendra K. Verma[1,2(b)]

[1] *Department of Physics, Indian Institute of Technology Kanpur - Kanpur 208016, India*
[2] *Kotak School of Sustainability, Indian Institute of Technology Kanpur - Kanpur 208016, India*

received 2 October 2025; accepted in final form 28 April 2026
published online 18 May 2026

Abstract – Modeling atmospheric and stellar phenomena requires understanding compressive turbulence, a more complex problem than its incompressible counterpart. This paper employs a novel mathematical framework to analyze energy transfers and fluxes in subsonic compressible flows. We perform direct numerical simulations on a 1024^3 grid for turbulent Mach numbers 0.15, 0.30, and 0.45. We apply stochastic random forcing to both rotational and compressive modes. We demonstrate that for subsonic flows, energy transfers from solenoidal to compressive modes are confined primarily to large scales, allowing independent rotational and compressive kinetic energy cascades. Consequently, both components maintain constant inertial-range fluxes, resulting in Kolmogorov scaling for the rotational velocity and Burgers scaling for the compressive velocity. We also observe that compressive kinetic energy is converted to internal energy via pressure dilatation. This advancement enables further exploration of locality, compressible convection, and compressible magnetohydrodynamics.

Introduction. – Flows in the planetary and stellar atmospheres, galaxies, astrophysical jets, compressors, and engines are turbulent and compressible [1,2]. Despite efforts over a century, many issues in such flows remain unresolved. For example, the energy spectra of compressible turbulence are reasonably well studied, but the energy fluxes are not. Kida and Orszag [3,4], Miura and Kida [5], Graham *et al.* [6], and Schmidt and Grete [7] have constructed energy fluxes for the compressible turbulence, but they do not provide detailed energy transfers among the compressive and solenoidal velocity components and the internal energy. Recently, Singh *et al.* [8] constructed a mathematical framework, an extension of *mode-to-mode energy transfers* for incompressible turbulence [9,10], that provides detailed energy transfers in compressible turbulence. We employ this formalism to the data obtained from direct numerical simulation and compute detailed energy fluxes for *subsonic compressible turbulence*. Our letter quantifies the energy fluxes by precisely identifying donor and receiver modes. This allows us to calculate inter-scale transfers, cross-transfers from solenoidal to compressive modes, and conversion to internal energy —thus improving upon previous works [1,6,7]. Our analysis is of critical importance for modelling the Earth's and Sun's atmospheres [11–14].

Incompressible turbulence theory is reasonably well developed [15]. The kinetic energy spectrum of incompressible turbulence follows Kolmogorov's spectrum, $E(k) = K_{\rm Ko}\epsilon^{2/3}k^{-5/3}$, where $K_{\rm Ko}$ is Kolmogorov's constant, and ϵ is the inertial-range energy flux, which equals the viscous dissipation rate [15–17]. Dar *et al.* [9], Kraichnan [18], and Verma [10] developed detailed energy transfers among the Fourier modes, including *triadic mode-to-mode energy transfers* that facilitate easy computation of energy fluxes and shell-to-shell energy transfers. In incompressible hydrodynamic turbulence, the maximal energy transfers occur between the neighboring wave number shells, a phenomenon referred to as *locality* [19–22]. Compared to incompressible turbulence, compressible turbulence theory is less developed. This study aims to contribute to this area by applying the recently developed formalism of Singh *et al.* [8] to compute detailed energy fluxes in subsonic flows.

Turbulent Mach number (M_t), which is the ratio of root-mean-square (rms) velocity (U) and the sound speed (C_s), is a measure of compressibility in a turbulent flow. Also, the *solenoidal or rotational* (divergence-free) and

(a) E-mail: tharshit@iitk.ac.in (corresponding author)
(b) E-mail: mkv@iitk.ac.in

compressive (curl-free) components of the velocity field behave quite differently in a compressible flow. For moderate Mach numbers, the rotational velocity component exhibits Kolmogorov's $k^{-5/3}$ spectrum, whereas the compressive component follows k^{-2} spectrum, which is attributed to the shocks [3,4,23–26]. In addition, compressible turbulence involves complex energy transfers among the velocity components and the internal energy. Kida and Orszag [3,4] and Miura and Kida [5] derived formulas for the cumulative energy transfers between the kinetic and internal energies. Using numerical simulations, they showed that the kinetic energies of the rotational and compressive components are transferred to the internal energy via viscous dissipation and pressure dilatation. Using numerical simulations, Jagannathan and Donzis [27], John and Donzis [28], Sarkar *et al.* [29], and Sarkar [30] studied the scaling of pressure dilation, viscous dissipation, and kinetic energy with M_t and Reynolds number. Interestingly, some of these quantities appear to depend on the forcing mechanism, *i.e.*, on the intensities of the rotational and compressive components [4,27].

Multiscale energy flux provides valuable insights into the turbulent dynamics. Graham *et al.* [6], Schmidt and Grete [7], and Grete *et al.* [31] derived expressions for the *spectral energy transfers* and shell-to-shell energy transfers for the *compressible magnetohydrodynamic turbulence*. They showed that energy transfers in compressible MHD are local; that is, the maximal energy transfers take place across nearest wave number shells. However, this compressible turbulence framework is less developed than its incompressible counterpart [9,10,18]. For example, Graham *et al.* [6] and Schmidt and Grete [7] do not discuss *mode-to-mode energy transfers* or *detailed energy conservation* in compressible turbulence, nor do they provide details of energy fluxes. We remark that accurate shell-to-shell energy transfers require the mode-to-mode energy transfer framework [9,32].

Recently, Singh *et al.* [8] extended the mode-to-mode energy transfer formalism of Dar *et al.* [9] to compute various energy transfers and fluxes of compressible flows. Singh *et al.* [8] derived formulas to calculate the energy fluxes for the rotational and compressive velocity components, as well as those related to the internal energy, pressure dilatation, and viscous dissipation. In this paper, we employ this framework to the simulation data and compute a variety of energy fluxes for *subsonic* compressible turbulence ($M_t < 1$). In particular, we compute the energy fluxes for Mach numbers $M_t = 0.15$, 0.30, and 0.45 using numerical data generated by a finite-difference code *Dhara* [33]. Our results show constant inertial-range fluxes for both velocity components, and a weak energy transfer from the solenoidal component to the compressive component.

Researchers have also computed the energy transfers in real space using subgrid-scaling (SGS) [23,34–36] and structure functions. Using SGS, Aluie [34,37] reported local energy cascade in compressible turbulence, whereas Aluie *et al.* [38] showed that the pressure dilatation acts primarily at large scales. Building on Kolmogorov's [16,17] work, Falkovich *et al.* [39], and Banerjee and Galtier [40], and Kritsuk *et al.* [41] have derived the structure functions for compressible turbulence. Sagaut and Cambon [42] studied pressure-strain correlations in compressible turbulence. Although the real-space description of compressible turbulence is outside the scope of this paper, we briefly compare our findings with existing real-space analyses.

Methods. – A compressible flow is characterised by the velocity field $\mathbf{u}$, density ρ, pressure σ, and internal energy I. In addition, we assume the fluid to be an ideal gas for which $\sigma = \rho R^* T$ and $I = \rho C_V T$, where T is the temperature, R^* is the gas constant, and C_V is the specific heat at constant volume [3]. See Supplementary Material `Supplementarymaterial.pdf` (SM) for the governing equations (and simulation setup, and additional numerical results). In this letter, we focus on the fluid kinetic energy (KE), $\rho u^2/2$, whose evolution equation is

$$\partial_t\left(\rho\frac{u^2}{2}\right)+\nabla\cdot\left(\rho\frac{u^2}{2}\mathbf{u}\right)+\mathbf{u}\cdot\nabla\sigma+\text{Viscous term}=\rho\mathbf{F}\cdot\mathbf{u}, \tag{1}$$

where $\mathbf{F}$ is the external force density that injects kinetic energy to the flow. The kinetic energy flux transfers the injected energy to small scales, where the kinetic energy is viscously dissipated and converted to internal energy. A fraction of the injected energy is transferred to the internal energy via pressure dilatation ($\mathbf{u}\cdot\nabla\sigma$).

We employ the formulas derived in Singh *et al.* [8] to compute the energy transfers in the flow. To make the kinetic energy ($\rho u^2/2$) quadratic, we rewrite it as $\mathbf{u}\cdot\mathbf{v}$ with $\mathbf{v}=\rho\mathbf{u}$ [6], leading to the modal energy as

$$E_u(\mathbf{k}) = \frac{1}{2}\Re\left[\mathbf{v}(\mathbf{k})\cdot\mathbf{u}^*(\mathbf{k})\right]. \tag{2}$$

An alternative is to use density-weighted velocity $\mathbf{w}=\sqrt{\rho}\mathbf{u}$ [3,5,7,43–46], with which $E_u(\mathbf{k})=|\mathbf{w}(\mathbf{k})|^2/2$. However, both transformations yield nearly the same results [6]. In addition to the kinetic energy spectrum ($E_u(\mathbf{k})$), we also calculate the density spectrum ($E_\rho(\mathbf{k})$), temperature spectrum ($E_T(\mathbf{k})$), and the internal energy spectrum ($I(\mathbf{k})$) defined as [47,48]

$$E_\rho(\mathbf{k}) = \frac{1}{2}|\rho(\mathbf{k})|^2, \tag{3}$$

$$E_T(\mathbf{k}) = \frac{1}{2}|T(\mathbf{k})|^2, \tag{4}$$

$$I(\mathbf{k}) = \frac{1}{\gamma(\gamma-1)M_0^2}\mathrm{Re}[\rho(\mathbf{k})T^*(\mathbf{k})]. \tag{5}$$

For further insights, we decompose the velocity field into its rotational component, $\mathbf{u}_R$, and compressible component, $\mathbf{u}_C$: $\mathbf{u}=\mathbf{u}_R+\mathbf{u}_C$ [3,32,42]. The corresponding modal energies are $E_\alpha(\mathbf{k})=\mathrm{Re}\big[\mathbf{v}_\alpha(\mathbf{k})\cdot\mathbf{u}_\alpha^*(\mathbf{k})\big]/2$, where $\alpha=R,C$ represent the rotational and compressional components, respectively. The evolution equations for these

modal energies are

$$\partial_t E_\alpha(\mathbf{k}) = \sum_{\mathbf{p}} S^{\alpha\alpha}(\mathbf{k}|\mathbf{p}|\mathbf{q}) + \sum_{\mathbf{p}} S^{\alpha\beta}(\mathbf{k}|\mathbf{p}|\mathbf{q}) - Q_{I,\alpha}(\mathbf{k}) - D_{I,\alpha}(\mathbf{k}) + \mathcal{F}_\alpha(\mathbf{k}), \quad (6)$$

where $\mathbf{k} = \mathbf{p} + \mathbf{q}$; $Q_{I,\alpha}(\mathbf{k})$ and $D_{I,\alpha}(\mathbf{k})$ are the energy transfers from $\mathbf{u}_\alpha$ to the internal energy via pressure dilatation and viscous dissipation, respectively; and $\mathcal{F}_\alpha(\mathbf{k})$ is the kinetic energy injection rate by the external force component $\mathcal{F}_\alpha$ (solenoidal or compressive). In $Q_{I,\alpha}(\mathbf{k})$ and $D_{I,\alpha}(\mathbf{k})$, the subscripts (I,α) denote energy transfers from $\mathbf{u}$ to the internal energy I. More importantly,

$$S^{\alpha\alpha}(\mathbf{k}|\mathbf{p}|\mathbf{q}) = \frac{1}{2}\mathrm{Im}\big[\{\mathbf{k}\cdot\mathbf{u}(\mathbf{q})\}\{\mathbf{v}_\alpha(\mathbf{p})\cdot\mathbf{u}^*_\alpha(\mathbf{k})\} + \{\mathbf{p}\cdot\mathbf{u}(\mathbf{q})\}\{\mathbf{u}_\alpha(\mathbf{p})\cdot\mathbf{v}^*_\alpha(\mathbf{k})\}\big] \quad (7)$$

is the *mode-to-mode energy transfer* from $\mathbf{u}_\alpha(\mathbf{p})$ to $\mathbf{u}_\alpha(\mathbf{k})$ with the mediation of $\mathbf{u}(\mathbf{q})$ (full $\mathbf{u}$); and

$$S^{\alpha\beta}(\mathbf{k}|\mathbf{p}|\mathbf{q}) = \frac{1}{2}\mathrm{Im}\big[\{\mathbf{k}\cdot\mathbf{u}(\mathbf{q})\}\{\mathbf{v}_\beta(\mathbf{p})\cdot\mathbf{u}^*_\alpha(\mathbf{k})\} + \{\mathbf{p}\cdot\mathbf{u}(\mathbf{q})\}\}\mathbf{u}_\beta(\mathbf{p})\cdot\mathbf{v}^*_\alpha(\mathbf{k})\}\big] \quad (8)$$

is the *mode-to-mode energy transfer* from $\mathbf{u}_\beta(\mathbf{p})$ to $\mathbf{u}_\alpha(\mathbf{k})$ with the mediation of $\mathbf{u}(\mathbf{q})$ ($\beta \neq \alpha$). That is, the rotational modes exchange energy among themselves via S^{RR} transfers, and so do the compressive modes via S^{CC} transfers. In addition, the rotational and compressive modes exchange energy via $S^{\alpha\beta}$ transfers. Also, $\mathbf{u}_\alpha(\mathbf{k})$ loses energy to I via pressure dilatation $Q_{I,\alpha}(\mathbf{k})$ and viscous dissipation $D_{I,\alpha}(\mathbf{k})$.

Using $S^{\alpha\alpha}(\mathbf{k}|\mathbf{p}|\mathbf{q})$, we can define energy flux $\Pi_\alpha(K)$, which is the net energy transfer from the $\mathbf{u}_\alpha$ modes inside the wave number sphere of radius K to the $\mathbf{u}_\alpha$ modes outside the sphere, that is,

$$\Pi_\alpha(K) = \Pi^{\alpha<}_{\alpha>}(K) = \sum_{k>K}\sum_{p\le K} S^{\alpha\alpha}(\mathbf{k}|\mathbf{p}|\mathbf{q}). \quad (9)$$

On the other hand, $S^{\alpha\beta}(\mathbf{k}|\mathbf{p}|\mathbf{q})$ helps define the following four energy fluxes related to the cross transfers:

$$\Pi^{R<}_{C<}(K) = \sum_{k\le K}\sum_{p\le K} S^{CR}(\mathbf{k}|\mathbf{p}|\mathbf{q}), \quad (10)$$

$$\Pi^{R>}_{C>}(K) = \sum_{k>K}\sum_{p>K} S^{CR}(\mathbf{k}|\mathbf{p}|\mathbf{q}), \quad (11)$$

$$\Pi^{R<}_{C>}(K) = \sum_{k>K}\sum_{p\le K} S^{CR}(\mathbf{k}|\mathbf{p}|\mathbf{q}) \quad (12)$$

$$\Pi^{C<}_{R>}(K) = \sum_{k>K}\sum_{p\le K} S^{RC}(\mathbf{k}|\mathbf{p}|\mathbf{q}) \quad (13)$$

Here, the superscripts and subscripts of Π represent the giver and receiver fields, respectively, whereas $<$ and $>$ represent wave number modes inside and outside the sphere, respectively [9,10]. In addition, $Q_{I,\alpha}, D_{I,\alpha}$, and $\mathcal{F}_\alpha$ yield the following fluxes:

$$\Pi^{\alpha<}_{I,Q}(K) = \sum_{k\le K} Q_{I,\alpha}(\mathbf{k}), \quad (14)$$

$$\Pi^{\alpha<}_{I,D}(K) = \sum_{k\le K} D_{I,\alpha}(\mathbf{k}), \quad (15)$$

$$\epsilon^{\mathrm{inj}}_\alpha = \sum_{k\in k_f} \mathcal{F}_\alpha(\mathbf{k}), \quad (16)$$

where k_f is the forcing wave number band, and $\epsilon^{\mathrm{inj}}_\alpha$ is the energy injection rate to the component α by the external force. Note that the total energy injection rate $\epsilon^{\mathrm{inj}} = \epsilon^{\mathrm{inj}}_R + \epsilon^{\mathrm{inj}}_C$. See fig. 1 for illustration of these fluxes, and Singh *et al.* [8] for further details.

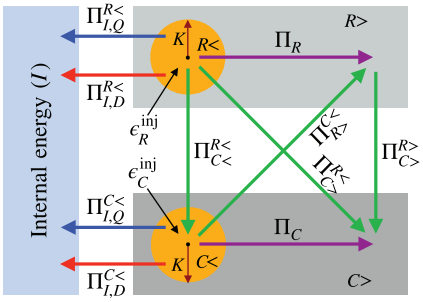

Fig. 1: Various fluxes in compressible turbulence: rotational and compressive energy fluxes (Π_R, Π_C), cross-fluxes ($\Pi^{R<}_{C<}, \Pi^{R<}_{C>}, \Pi^{R>}_{C>}, \Pi^{C<}_{R>}$), pressure dilatation ($\Pi^R_{I,Q}, \Pi^C_{I,Q}$), viscous dissipation ($\Pi^R_{I,D}, \Pi^C_{I,D}$), and energy injection rates by the external force ($\epsilon^{\mathrm{inj}}_R, \epsilon^{\mathrm{inj}}_C$).

Results. – We simulate the nondimensionalized equations of compressible hydrodynamics in conservative form using *Dhara* [33], which is a finite-difference code employing computationally-efficient MacCormack scheme [49,50]. For unforced equations, the solver conserves mass and total energy, which we have verified numerically. In addition, we validated the code using Kida and Orszag's [3] results.

We performed three sets of compressible turbulence simulations on a 1024^3 uniform grid using Kida and Orszag's [3] forcing scheme with equal forcing amplitudes for the rotational and compressive velocity components. For all the runs, we set $\mathrm{Pr} = 1$ and $M_0 = 1$. To maintain a statistically steady state, we employ a nearly isothermal equation of state with $\gamma = 1.001$ [26,51]. In forced simulations, viscous dissipation continuously converts kinetic energy into internal energy, increasing the temperature and sound speed over time. This inevitably reduces the turbulent Mach number, preventing a steady state unless an artificial cooling term is introduced. The choice of $\gamma = 1.001$ effectively mimics isothermal conditions, preventing this continuous temperature rise and allowing us to focus on the steady-state statistics without introducing additional cooling parameters or timescales [26,51].

We set the initial conditions as $\rho(t=0) = T(t=0) = 1$ and $\mathbf{u}(t=0) = 0$ and simulate up to 150 eddy turnover

Table 1: Simulation parameters for the three runs: the forcing parameters (f_R, f_C), the reference Reynolds number (Re_0), Taylor microscale Reynolds number (Re_λ), and the turbulent Mach number (M_t).

Run	f_R	f_C	Re_0	Re_λ	M_t
1	1.5×10^{-4}	1.5×10^{-4}	1.5×10^{4}	277	0.15
2	7.5×10^{-4}	7.5×10^{-4}	1×10^{4}	328	0.30
3	4×10^{-3}	4×10^{-3}	0.5×10^{4}	259	0.45

times (l_0/u_0), ensuring that the system has reached a statistically steady state. The reference Reynolds number (Re_0) and resulting steady-state properties for the three runs are summarized in table 1. The simulations resulted in Taylor-scale Reynolds numbers (Re_λ) 277, 328, and 259, with corresponding turbulent Mach numbers (M_t) of 0.15, 0.30, and 0.45, respectively. The range of Re_λ achieved in our simulations for the corresponding Mach numbers is comparable to those of other high-resolution studies [27,35,52,53]. See SM for further details. Our simulations are well resolved, as $\eta/(\Delta x) > 1$, where η is Kolmogorov's length [27]. See table 1 of the SM for the numerical values. Our parallel run took around 48 hours on the Kotak school's server with 8 H100 GPUs.

Energy spectra. The average Mach numbers for the three runs are 0.15, 0.30, and 0.45 which are relevant for studies of terrestrial and solar atmospheres [11–14]. We present the energy spectra and energy fluxes for these runs. Figure 2 presents the energy spectra and fluxes for $M_t = 0.45$, whereas fig. 1 of the SM presents these quantities for $M_t = 0.15$ and 0.30. Our forcing band at $k = 1$ ensures a clean separation between the energy injection scales and the inertial range [54]. To isolate the inertial range from the forcing band, the spectral exponents are calculated using fits restricted to wave numbers $k \geq 4$. Furthermore, our setup yields large Taylor-scale Reynolds numbers ($\mathrm{Re}_\lambda \approx 250$ to 350), which guarantees a wide inertial range well separated from the dissipation scales [52,53]. As shown in fig. 2(a), the rotational kinetic energy spectrum $E_R(k)$ follows Kolmogorov's $k^{-5/3}$ scaling, while the compressive energy spectrum $E_C(k)$ follows the k^{-2} Burgers spectrum associated with shocks [24,25,55,56]. The k^{-2} scaling arises from shock discontinuities, rather than vortex stretching or pressure-strain redistribution, similar to the Burgers turbulence. Since $E_R(k) \gg E_C(k)$, the total energy spectrum $E_u(k)$ too scales as $k^{-5/3}$. Since density, temperature, and internal energy are coupled to the compressive velocity, they exhibit k^{-2} scaling. Interestingly, $E_C(k) \approx E_\rho(k)$ for subsonic turbulence. We will investigate the reason for this similarity in the future. These results are consistent with earlier works [3,7,23,48,53].

Energy fluxes. Next, we present the energy fluxes of compressible turbulence. We normalize the energy fluxes

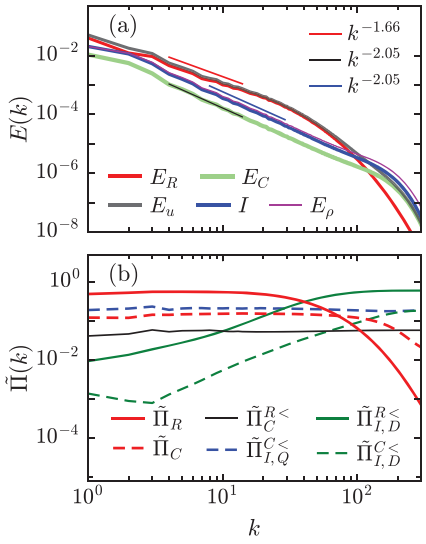

Fig. 2: For $M_t = 0.45$, (a) Energy spectra: $E_R(k)$, $E_C(k)$, $E_u(k)$, $I(k)$, $E_\rho(k)$ and $2\times10^5 E_T(k)$. Dashed lines represent $k^{-5/3}$ and k^{-2} fits. (b) Normalized energy fluxes $\tilde{\Pi}_R(k), \tilde{\Pi}_C(k)$, $\tilde{\Pi}_{I,D}^{R<}(k)$, $\tilde{\Pi}_C^{R<}(k)$, $\tilde{\Pi}_{I,Q}^{C<}(k)$, and $\tilde{\Pi}_{I,D}^{C<}(k)$. Note that $\tilde{\Pi}_R(k), \tilde{\Pi}_C(k)$, and $\tilde{\Pi}_{I,Q}^{C<}(k)$ are constant in the inertial range.

of eqs. (9)–(15) by the total injection rate ϵ^{inj}. These normalized fluxes, denoted by tilde, are presented in fig. 2(b) (for $M_t = 0.45$), and their maxima in fig. 3(c). As shown in fig. 2(b), the normalized energy fluxes of the velocity components, $\tilde{\Pi}_R(K)$ and $\tilde{\Pi}_C(k)$, are constant in the inertial range ($4 \lessapprox k \lessapprox 15$). These fluxes are viscously dissipated and transferred to the internal energy, as shown in fig. 3. For the rotational component, the Kolmogorov constant $K_{\mathrm{Ko}} = E_R(k)k^{5/3}(\Pi_R)^{-2/3} \approx 2$, which is near that for incompressible turbulence [15]. These observations indicate that the rotational component follows the dynamics of incompressible turbulence.

Figure 2(b) and fig. 3 also show that for the compressive component, the pressure dilatation flux $\tilde{\Pi}_{I,Q}^{C<}(k)$ is of the order of the compressive viscous dissipation. Since $\tilde{\Pi}_{I,Q}^{C<}(k)$ is nearly constant in k, the pressure dilatation is active at small wave numbers or at large length scales. In addition, $\tilde{\Pi}_{I,Q}^{R<}(k) \approx 0$, indicating that the pressure does not induce significant energy transfer for the rotational component, which is consistent with the theories of incompressible turbulence [10,32]. Lastly, $\tilde{\Pi}_{C<}^{R<}(k) \approx 0.02$ to 0.06 for small k, indicating a small energy transfer from $\mathbf{u}_R$ to $\mathbf{u}_C$ at large length scales (see fig. 3). The energy fluxes of eqs. (11)–(13) are negligible. The small cross-transfers have insignificant impact on $\tilde{\Pi}_R(k)$ and $\tilde{\Pi}_C(k)$, which makes these fluxes constant in the inertial range [57].

Figure 3 also illustrates how the energy fluxes vary with Mach number, at least in the range from 0.15 to 0.45. As M_t increases, the rotational flux $\tilde{\Pi}_R(k)$ decreases, while the compressive flux $\tilde{\Pi}_C(k)$ remains nearly unchanged. This feature correlates with the decrease in the rotational

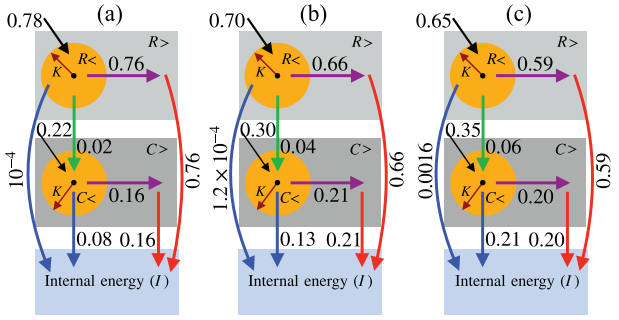

Fig. 3: For (a) $M_t = 0.15$, (b) $M_t = 0.30$, (c) $M_t = 0.45$: schematic diagrams showing energy fluxes from a wave number sphere of radius K (K in the inertial range). The normalized energy injection rates $\tilde{\epsilon}_R^{\rm inj}, \tilde{\epsilon}_C^{\rm inj}$; maxima of normalized fluxes $\tilde{\Pi}_R(k), \tilde{\Pi}_C(k), \tilde{\Pi}_{C<}^{R<}(k), \tilde{\Pi}_{I,Q}^{C<}(k), \tilde{\Pi}_{I,Q}^{R<}(k)$; and total normalized dissipation rates $\tilde{\epsilon}_R, \tilde{\epsilon}_C$.

injection rate $\tilde{\epsilon}_R^{\rm inj}$ and the increase in the compressive injection rate $\tilde{\epsilon}_C^{\rm inj}$ as M_t increases. The pressure dilatation for the compressive component $\tilde{\Pi}_{I,Q}^{C<}(k)$ increases with M_t, indicating enhanced compressive activity at higher Mach numbers.

Note that the nature of the forcing significantly affects the energy cascade in compressible turbulence [3,7]. In the subsonic regime, the total and solenoidal kinetic energy spectra are nearly unaffected by the forcing, while the compressive spectrum is highly sensitive to it. Furthermore, the energy fluxes depend heavily on the solenoidal-to-compressive forcing ratio: the solenoidal flux dominates under purely solenoidal forcing, and the compressive flux dominates under purely compressive forcing [3,7,23,27,35]. Although all the simulations in this study utilize a mixed forcing ($\epsilon_R^{\rm inj}/\epsilon_C^{\rm inj} \approx 2$), we also performed sensitivity tests using purely solenoidal and purely compressive forcing on smaller grids, similarly to Kida and Orszag [3]. Our results are consistent with these previous findings [3,7,27,35].

Comparison with past works. – We compare our findings to real-space flux analyses by Wang *et al.* [35] and Wang *et al.* [23], which utilized Favre filtering and Helmholtz decomposition. Our simulations, which use mixed forcing ($\epsilon_R^{\rm inj}/\epsilon_C^{\rm inj} \approx 2$), show clear differences from the purely rotationally forced case in [35]. Specifically, we find that $\tilde{\Pi}_R$ decreases with increasing M_t, rather than remaining constant. Additionally, the cross-transfer between rotational and compressive components occurs primarily at large scales —unlike the all-scale-transfer reported in [35]. This is the primary reason for the observed independent cascades of rotational and compressive KE. Furthermore, the pressure dilatation flux, which they found to be very small and active at all scales, is both significant and predominantly active at large scales in our work.

The differences from Wang *et al.* [35] arises primarily due to the forcing setup and the mathematical methodology used to calculate energy fluxes. The large-scale rotational forcing used in Wang *et al.* [35] produces weak dilatational velocity. This leads to weak pressure dilatation and compressible flux, which increase with M_t but remain significantly smaller than the solenoidal flux. Consequently, KE cascades almost entirely through the solenoidal flux and is ultimately dissipated by solenoidal viscous dissipation. Thus, the normalized solenoidal flux ($\tilde{\Pi}_R$) remains nearly constant in Wang *et al.* [35] even as M_t increases. Furthermore, since the compressive modes receive no direct energy injection, they absorb energy from the solenoidal cascade via nonlinear cross-transfer across all length scales [35].

In contrast, our mixed forcing injects energy into both rotational and compressive modes. This generates strong dilatational velocity at the forcing scales, yielding substantial large-scale pressure dilatation and compressive flux. Crucially, as M_t increases, pressure dilatation grows significantly, and a larger fraction of the injected KE is converted into internal energy at large scales. This correlates with a decrease in the rotational injection rate ($\tilde{\epsilon}_R^{\rm inj}$) and a corresponding increase in the compressive injection rate ($\tilde{\epsilon}_C^{\rm inj}$). Consequently, the amount of energy available to cascade down the solenoidal inertial range shrinks, causing $\tilde{\Pi}_R$ to decrease steadily.

Our results also diverge from the mixed-forcing study of Wang *et al.* [23], where $\tilde{\Pi}_C \gg \tilde{\Pi}_R$. We consistently observe $\Pi_C < \Pi_R$ for all M_t, with a comparable pressure flux $\tilde{\Pi}_{I,Q}^{C<}$. Wang *et al.* [23] linked their dominant $\tilde{\Pi}_C$ to the $k^{-5/3}$ scaling of the total energy spectrum. In our work, however, this $k^{-5/3}$ scaling is recovered even with a sub-dominant compressive flux $\tilde{\Pi}_C$.

Methodologically, real-space analyses [23,35–37] rely on Favre-filtered velocity fields, which provide excellent spatial locality but inherently couple kinematic and thermodynamic fluctuations. Furthermore, decomposed real-space kinetic energy fluxes capture the net energy transfer across a scale, but they do not explicitly isolate the specific triadic pathways (*i.e.*, whether the energy leaving a large-scale solenoidal mode is transferred to small-scale solenoidal or compressive modes) [23,35]. In contrast, our formalism utilizes shell-to-shell transfers to precisely identify the donor and receiver modes. This enables the exact calculation of energy transfer between modes, revealing that the kinetic cross-transfers and pressure dilatation are actually confined primarily to the large scales.

Conclusions. – Quantifying the energy transfer between solenoidal and dilatational motions remains a central problem in compressible turbulence. This paper presents a major advancement by providing a precise characterization of these energy transfers within the moderately compressible regime —a regime relevant to the Earth's and Sun's atmospheres. We employ the formulas derived in Singh *et al.* [8] to the DNS data and compute various energy transfers for subsonic compressible turbulence for turbulent Mach numbers 0.15, 0.30, and 0.45. The precise identification of donor and receiver modes

allows calculation of both inter-scale and cross-transfers among different energy modes, providing a comprehensive picture of the energy cascade.

Using the numerical data, we compute various energy spectra and fluxes and global quantities —the total kinetic energy, pressure dilatation, and dissipation rates. We show that the rotational component exhibits Kolmogorov's $k^{-5/3}$ spectrum, whereas the compressive component exhibits a Burgers k^{-2} spectrum, both with constant energy fluxes. There is a weak energy transfer from the solenoidal to the compressive velocity modes predominantly at large scales. In addition, pressure dilation converts the kinetic energy to internal energy mostly along the compressive velocity channel. This mechanism is also found to be confined to the large scales. Since both the cross-transfer and pressure dilatation occur at large scales, the rotational and compressive KE cascades are largely independent. This allows the rotational component to follow a Kolmogorov-like cascade and the compressive component to follow a Burgers-like cascade. These findings provide a more quantitative understanding of the energy transfer mechanisms in subsonic turbulence.

The nature of forcing plays a critical role in compressible turbulence [3,27]. Hence, we will explore how the energy fluxes vary with different types of forcing and with the Mach number. The energy transfers for supersonic compressible turbulence ($M_t > 1$) may show different properties, which will be investigated in the near future.

Our study provides a detailed characterization of energy transfers for subsonic flows. In future, we plan to study supersonic turbulence in high-speed aerodynamics [58], supernova explosions, and star formation [59,60]. We also propose to study shell-to-shell energy transfers in detail so as to quantify locality in compressible turbulence [20,21,61,62]. A simple generalization of the present formulation will provide accurate models for compressible convection [63], quantum turbulence [64], and compressible magnetohydrodynamics [7].

* * *

The authors thank Rajesh Ranjan, Fahad Anwar, Sanjiva Lele, Parviz Moin, Manthan Verma, Abhishek Jha, Shashwat Nirgudkar, and Abhay Kumar for useful discussions. Simulations were performed on the HPC cluster of Kotak School of Sustainability (KSS), IIT Kanpur. LS thanks IITK for the Institute Postdoctoral Fellowship. Part of this work was done in the Center for Turbulence Research, Stanford University, where MKV was a Visiting Senior Fellow. Part of this work was supported by Anusandhan National Research Foundation, India (SERB/PHY/2021522) and the J. C. Bose Fellowship (SERB/PHY/2023488).

Data availability statement: The data that support the findings of this study will be openly available following an embargo at the following URL/DOI: `https://zenodo.org/records/20150962`.

REFERENCES

[1] Lele S. K., *Annu. Rev. Fluid Mech.*, **26** (1994) 211.
[2] Carroll B. W., *An Introduction to Modern Astrophysics*, 2nd edition (Pearson) 2006.
[3] Kida S. and Orszag S. A., *J. Sci. Comput.*, **5** (1990) 85.
[4] Kida S. and Orszag S. A., *J. Sci. Comput.*, **7** (1992) 1.
[5] Miura H. and Kida S., *Phys. Fluids*, **7** (1995) 1732.
[6] Graham J. P., Cameron R. and Schüssler M., *Astrophys. J.*, **714** (2010) 1606.
[7] Schmidt W. and Grete P., *Phys. Rev. E*, **100** (2019) 043116.
[8] Singh D., Tiwari H., Sharma L. and Verma M. K., *Phys. Rev. Fluids*, **10** (2025) 114609.
[9] Dar G., Verma M. K. and Eswaran V., *Physica D*, **157** (2001) 207.
[10] Verma M. K., *Phys. Rep.*, **401** (2004) 229.
[11] Fritts D. C. and Alexander M. J., *Rev. Geophys.*, **41** (2003) 1003.
[12] Spruit H. C., Nordlund A. and Title A. M., *Annu. Rev. Astron. Astrophys.*, **28** (1990) 263.
[13] Nordlund A. and Stein R. F., *Living Rev. Sol. Phys.*, **6** (2009) 2.
[14] Carlsson M., De Pontieu B. and Hansteen V. H., *Annu. Rev. Astron. Astrophys.*, **57** (2019) 189.
[15] Lesieur M., *Turbulence in Fluids* (Springer-Verlag, Dordrecht) 2008.
[16] Kolmogorov A. N., *Dokl. Acad. Nauk SSSR*, **32** (1941) 16.
[17] Kolmogorov A. N., *Dokl. Acad. Nauk SSSR*, **30** (1941) 301.
[18] Kraichnan R. H., *J. Fluid Mech.*, **5** (1959) 497.
[19] Domaradzki J. A. and Rogallo R. S., *Phys. Fluids A*, **2** (1990) 414.
[20] Zhou Y., *Phys. Fluids*, **5** (1993) 1092.
[21] Zhou Y., *Phys. Fluids A*, **5** (1993) 2511.
[22] Verma M. K., Ayyer A., Debliquy O., Kumar S. and Chandra A. V., *Pramana-J. Phys.*, **65** (2005) 297.
[23] Wang J., Yang Y., Shi Y., Xiao Z., He X. T. and Chen S., *Phys. Rev. Lett.*, **110** (2013) 214505.
[24] Burgers J. M., *Adv. Appl. Mech.*, **1** (1948) 171.
[25] Saffman P. G., in *Topics in Nonlinear Physics*, edited by Zabusky N. J. (Springer-Verlag, Berlin) 1968, pp. 485–614.
[26] Kritsuk A. G., Norman M. L., Padoan P. and Wagner R., *Astrophys. J.*, **665** (2007) 416.
[27] Jagannathan S. and Donzis D. A., *J. Fluid Mech.*, **789** (2016) 669.
[28] John J. P. and Donzis D. A., *Phys. Fluids*, **36** (2024) 106121.
[29] Sarkar S., Erlebacher G., Hussaini M. Y. and Kreiss H. O., *J. Fluid Mech.*, **227** (1991) 473.
[30] Sarkar S., *Phys. Fluids A*, **4** (1992) 2674.
[31] Grete P., O'Shea B. W., Beckwith K., Schmidt W. and Christlieb A., *Phys. Plasmas*, **24** (2017) 092311.
[32] Verma M. K., *Energy Transfers in Fluid Flows: Multiscale and Spectral Perspectives* (Cambridge University Press, Cambridge) 2019.
[33] Tiwari H., Sharma L. and Verma M. K., *Int. J. Heat Mass Transf.*, **242** (2025) 126821.
[34] Aluie H., *Phys. Rev. Lett.*, **106** (2011) 174502.

[35] Wang J., Wan M., Chen S. and Chen S., *J. Fluid Mech.*, **841** (2018) 581.
[36] Luo C., Fang L., Fang J., Xu H., Pumir A. and Yang P.-F., *J. Fluid Mech.*, **1018** (2025) A7.
[37] Aluie H., *Phys. D: Nonlinear Phenom.*, **247** (2013) 54.
[38] Aluie H., Li S. and Li H., *Astrophys. J.*, **751** (2012) L29.
[39] Falkovich G., Fouxon I. and Oz Y., *J. Fluid Mech.*, **644** (2010) 465.
[40] Banerjee S. and Galtier S., *J. Fluid Mech.*, **742** (2014) 230.
[41] Kritsuk A. G., Wagner R. and Norman M. L., *J. Fluid Mech.*, **729** (2013) R1.
[42] Sagaut P. and Cambon C., *Homogeneous Turbulence Dynamics*, 2nd edition (Cambridge University Press, Cambridge) 2018.
[43] Yih C.-S., *J. Fluid Mech.*, **9** (1960) 68.
[44] Zhou Y., *Phys. Rep.*, **720-722** (2017) 1.
[45] Zhou Y., Sadler J. D. and Hurricane O. A., *Annu. Rev. Fluid Mech.*, **57** (2025) 197.
[46] Rodriguez Azara J. and Emanuel G., *Phys. Fluids*, **31** (1988) 1058.
[47] Wang J., Gotoh T. and Watanabe T., *Phys. Rev. Fluids*, **2** (2017) 013403.
[48] Wang J., Wan M., Chen S., Xie C. and Chen S., *Phys. Rev. E*, **97** (2018) 043108.
[49] Wesseling P., *Principles of Computational Fluid Dynamics*, 1st edition (Springer-Verlag, Berlin, Heidelberg) 2000.
[50] Ouyang C., He S., Xu Q., Luo Y. and Zhang W., *Comput. Geosci.*, **52** (2013) 1.
[51] Falkovich G. and Kritsuk A. G., *Phys. Rev. Fluids*, **2** (2017) 092603(R).
[52] Zhou Y., *Hydrodynamic Instabilities and Turbulence: Rayleigh-Taylor, Richtmyer-Meshkov, and Kelvin-Helmholtz Mixing* (Cambridge University Press, Cambridge) 2024.
[53] Sakurai Y. and Ishihara T., *Phys. Fluids*, **36** (2024) 085152.
[54] Domaradzki J. A., Teaca B. and Carati D., *Phys. Fluids*, **22** (2010) 051702.
[55] Verma M. K., *Phys. A: Stat. Mech. Appl.*, **277** (2000) 359.
[56] Bec J. and Khanin K., *Phys. Rep.*, **447** (2007) 1.
[57] Verma M. K., *J. Phys. A: Math. Theor.*, **55** (2022) 013002.
[58] von Kármán T., *J. Spacecraft Rockets*, **40** (2003) 992.
[59] Krumholz M. R. and McKee C. F., *Astrophys. J.*, **630** (2005) 250.
[60] Padoan P. and Nordlund Å., *Astrophys. J.*, **730** (2011) 40.
[61] Kraichnan R. H., *J. Fluid Mech.*, **47** (1971) 525.
[62] Zhou Y., *Phys. Rep.*, **935** (2021) 1.
[63] Schumacher J. and Sreenivasan K. R., *Rev. Mod. Phys.*, **92** (2020) 041001.
[64] Barenghi C. F., Skrbek L. and Sreenivasan K. R., *Proc. Natl. Acad. Sci. U.S.A.*, **111** (4647) 2014.

Supplementary Material for "Scale-by-Scale Energy Transfers and Fluxes in Compressible Turbulence"

Dhananjay Singh,[1] Harshit Tiwari,[1] Lekha Sharma,[1] and Mahendra K. Verma[1,2]
[1]*Department of Physics, Indian Institute of Technology Kanpur, Kanpur 208016, India*
[2]*Kotak School of Sustainability, Indian Institute of Technology Kanpur, Kanpur 208016, India*
(Dated: February 25, 2026)

I. GOVERNING EQUATIONS

The nondimensional equations for compressible flow are [1]:

$$\frac{\partial \rho}{\partial t} + \frac{\partial}{\partial x_i}(\rho u_i) = 0, \tag{1}$$

$$\frac{\partial}{\partial t}(\rho u_i) + \frac{\partial}{\partial x_j}(\rho u_i u_j + \delta_{ij}\sigma - \tau_{ij}) = \rho F_i, \tag{2}$$

$$\frac{\partial E_T}{\partial t} + \frac{\partial}{\partial x_i}\left(u_i(E_T+\sigma) - \frac{1}{M_0^2 \mathrm{Pr}\mathrm{Re}_0(\gamma-1)}\frac{\partial T}{\partial x_i} - u_j\tau_{ij}\right) = \rho u_i F_i, \tag{3}$$

where ρ, $\mathbf{u}$, σ, T, and $\mathbf{F}$ are the density, velocity, pressure, temperature, and external force, respectively. These equations are made dimensionless using reference density ρ_0, temperature T_0, velocity u_0, and length l_0. The dimensionless parameters of the system are [1, 2]:

$$\text{Reynolds number} \quad \mathrm{Re}_0 = \frac{\rho_0 u_0 l_0}{\mu}, \tag{4}$$

$$\text{Reynolds number (Taylor microscale)} \quad \mathrm{Re}_\lambda = \left(\frac{5}{3\mu\epsilon}\right)^{1/2}\rho_0 U^2, \tag{5}$$

$$\text{Mach number} \quad M_0 = \frac{u_0}{C_s} = \frac{u_0}{\sqrt{\gamma R^* T_0}}, \tag{6}$$

$$\text{Turbulent Mach number} \quad M_t = \frac{U}{C_s}, \tag{7}$$

$$\text{Prandtl number} \quad \mathrm{Pr} = \frac{\mu C_p}{K_c}, \tag{8}$$

where U is the root mean square velocity, C_s is the sound speed, R^* is the gas constant, μ is the dynamic viscosity, ϵ is the mean viscous dissipation rate, and K_c is the thermal conductivity. In the Eqs. (1-3), $\tau_{ij} = \left(\partial_j u_i + \partial_i u_j - \frac{2}{3}\partial_m u_m \delta_{ij}\right)/\mathrm{Re}_0$ is the viscous stress tensor and E_T is the total energy density consisting of kinetic energy density, $E_u = \rho u^2/2$, and internal energy density, $I = \sigma/(\gamma-1)$, with $\gamma = C_p/C_v$ as the ratio of specific heat capacities at constant pressure and volume. The fluid also follows the ideal gas equation of state $\sigma = \rho T/(\gamma M_0^2)$.

II. SIMULATION DETAILS

We simulate the Eqs. (1-3) using the finite-difference GPU-enabled Python code *Dhara* [3]. We perform direct numerical simulations in a $(2\pi)^3$ periodic domain with a uniform collocation grid of 1024^3 points. For faster convergence, we apply sequential grid upscaling: starting from a 256^3 grid, the flow is evolved to a steady state and interpolated successively to finer grids until 1024^3 is reached. We used a Courant–Friedrichs–Lewy (CFL) number of 0.5, giving a time step of roughly $dt \approx 10^{-3}$.

Following the scheme proposed by Kida and Orszag [1], we employ random force on the velocity field at large scales. We choose the force component F_i as

$$F_i(\mathbf{x}, t) = A_{ij}(t)\sin x_j + B_{ij}(t)\cos x_j, \tag{9}$$

TABLE I. Numerically-computed rotational kinetic energy (E_R), compressive kinetic energy (E_C), their ratio E_R/E_C, Reynolds number based on Taylor microscale (Re_λ), resolution parameter ($\eta/\Delta x$), energy injection rates ($\epsilon_R^{\mathrm{inj}}, \epsilon_C^{\mathrm{inj}}$), normalized injection rates ($\tilde{\epsilon}_R^{\mathrm{inj}}$,$\tilde{\epsilon}_C^{\mathrm{inj}}$), normalized fluxes in the inertial range ($k = 10$), the Kolmogorov constants (K_{Ko}) for rotational kinetic energy, and the scaling exponents α for various energy spectra, along with their trends with increasing turbulent Mach numbers (M_t).

M_t	0.15	0.30	0.45	Trend with M_t
E_R	8.18×10^{-3}	3.51×10^{-2}	9.50×10^{-2}	Increases
E_C	1.80×10^{-3}	8.60×10^{-3}	2.90×10^{-2}	Increases
E_R/E_C	4.53	4.07	3.28	Decreases
Re_λ	277	328	259	-
$\eta/\Delta x$	1.14	1.01	1.11	-
$\epsilon_R^{\mathrm{inj}}$	1.37×10^{-4}	1.01×10^{-3}	4.19×10^{-3}	Increases
$\epsilon_C^{\mathrm{inj}}$	3.94×10^{-5}	4.26×10^{-4}	2.28×10^{-3}	Increases
$\tilde{\epsilon}_R^{\mathrm{inj}}$	0.78	0.70	0.65	Decreases
$\tilde{\epsilon}_C^{\mathrm{inj}}$	0.22	0.30	0.35	Increases
$\tilde{\Pi}_R \approx \tilde{\epsilon}_R$	0.76	0.66	0.59	Decreases
$\tilde{\Pi}_C \approx \tilde{\epsilon}_C$	0.16	0.21	0.20	Nearly constant
$\tilde{\Pi}_C^{R<}$	0.02	0.04	0.06	Marginally increases
$-\tilde{\Pi}_R^{C<}$	0.02	0.04	0.06	Marginally increases
$\tilde{\Pi}_{I,Q}^{R<}$	10^{-4}	1.2×10^{-4}	1.6×10^{-3}	Small, Increases
$\tilde{\Pi}_{I,Q}^{C<}$	0.08	0.13	0.21	Increases
K_{Ko}	2.12	2.14	2.02	Constant
α_R	-1.67 ± 0.035	-1.66 ± 0.021	-1.66 ± 0.025	-
α_C	-2.02 ± 0.009	-2.07 ± 0.009	-2.07 ± 0.004	-
α_u	-1.67 ± 0.027	-1.69 ± 0.018	-1.71 ± 0.022	-
α_I	-2.02 ± 0.005	-2.06 ± 0.007	-2.09 ± 0.006	-
α_ρ	-2.02 ± 0.007	-2.01 ± 0.006	-2.03 ± 0.006	-
α_T	-2.04 ± 0.004	-2.07 ± 0.009	-2.08 ± 0.007	-

where $i, j = 1, 2, 3$; $A_{ij}(t)$ and $B_{ij}(t)$ are Gaussian random variables with zero mean. The second-order moments are chosen as [1]

$$\overline{A_{ij}^2} = \overline{B_{ij}^2} = \begin{cases} \frac{f_C}{3dt} & \text{if } i = j, \\ \frac{f_R}{3dt} & \text{if } i \neq j, \end{cases} \tag{10}$$

where the parameters f_C and f_R control the power injected into the compressive and rotational components of the forcing, respectively, and Δt is the time-step. The specific values for these parameters are listed in Table 1 of the main Text. The resulting mean energy injection rate in the system is

$$\epsilon_{\mathrm{inj}} \approx \langle \rho \rangle \left(f_R + \frac{f_C}{2} \right). \tag{11}$$

In our simulation, we set the amplitudes of the rotational and compressive forcing components to be equal ($f_R = f_C$), which results in $\epsilon_R^{\mathrm{inj}}/\epsilon_C^{\mathrm{inj}} \approx 2$. Our runs are well resolved because $\eta/\Delta x \geq 1$ (see Table I), where

$$\eta = \left(\frac{\langle \mu \rangle^3}{\epsilon \langle \rho \rangle^2} \right)^{1/4} \tag{12}$$

is the Kolmogorov's length with $\langle \rho \rangle$ and $\langle \mu \rangle$ as the average density and dynamic viscosity, respectively [2].

In Table I, we list the total kinetic energy of $\mathbf{u}_{R,C}$ (E_R, E_C), the respective injection rates $(\epsilon_R^{\rm inj},\ \epsilon_C^{\rm inj})$, the ratio E_R/E_C, Reynolds number based on Taylor microscale (Re_λ), and the resolution parameter $(\eta/\Delta x)$ for the three runs. Note that the internal energy (≈ 1000) dominates the rotational and compressive kinetic energies. The table also lists the respective normalized energy fluxes (normalized with the total injection rates) and Kolmogorov's constants. The last six rows of the table contains the spectral exponents $\alpha_R, \alpha_C, \alpha_u, \alpha_I$, α_ρ, and α_T for $E_R(k), E_C(k), E_u(k), E_I(k)$, $E_\rho(k)$, and $E_T(k)$ respectively. The maximum errors in the spectral exponents are 2%, 1%, and 2% for $M_t = 0.15$, 0.30, and 0.45, respectively.

III. ENERGY SPECTRA AND FLUXES

Figure 2 of the main text exhibits the energy spectra and fluxes for $M_t = 0.45$. Figure 1(a,b) of this supplement show the spectra for $M_t = 0.15$ and 0.30, whereas Fig. 1(c,d) exhibits the corresponding energy fluxes. The spectral exponents for various energy spectra are listed in Table I. The behaviour of the energy spectra and fluxes for $M_t = 0.15, 0.30$, and 0.45 are very similar, and they follow trends discussed in the Main Text.

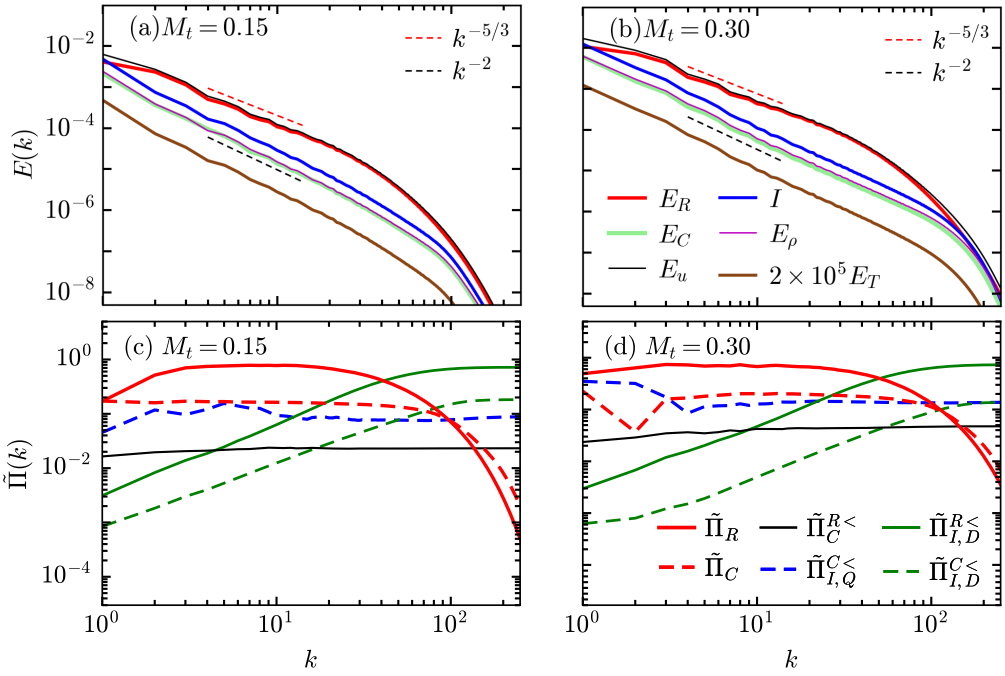

FIG. 1. For $M_t = 0.15$ (a,c) and $M_t = 0.30$ (b,d): (a,b) Energy spectra for rotational kinetic energy $E_R(k)$ (red), compressive kinetic energy $E_C(k)$ (light green), total kinetic energy $E_u(k)$ (dark gray), internal energy $I(k)$ (blue), density $E_\rho(k)$ (magenta), and normalized temperature $2 \times 10^5 E_T$ (brown). Dashed lines represent $k^{-5/3}$ and k^{-2} fits. (c,d) Normalized energy fluxes for the rotational component $\tilde{\Pi}_R(k)$ (solid red) and its dissipation $\tilde{\Pi}_{I,D}^{R<}(k)$ (solid green), the compressive component $\tilde{\Pi}_C(k)$ (dashed red) and its dissipation $\tilde{\Pi}_{I,D}^{C<}(k)$ (dashed green), cross transfer from $\mathbf{u}_R$ to $\mathbf{u}_C$, $\tilde{\Pi}_C^{R<}(k)$ (solid black), and compressive pressure-dilatation $\tilde{\Pi}_{I,Q}^{C<}(k)$ (dashed blue). Note that $\tilde{\Pi}_{I,Q}^{R<}(k) \approx 0$.

To further illustrate these scaling trends, Fig. 2(a,b) presents the rotational and compressible energy spectra compensated by $k^{5/3}$ and k^2, respectively. The compensated spectra remain nearly constant in their respective inertial ranges. Note that the inertial range for the compressible spectra, $k \in [4, 50]$, extends farther than that of the rotational spectra, $k \in [4, 25]$.

[1] S. Kida and S. A. Orszag, Energy and spectral dynamics in forced compressible turbulence, J. Sci. Comput. **5**, 85 (1990).
[2] S. Jagannathan and D. A. Donzis, Reynolds and Mach number scaling in solenoidally-forced compressible turbulence using high-resolution direct numerical simulations, J. Fluid Mech. **789**, 669 (2016).

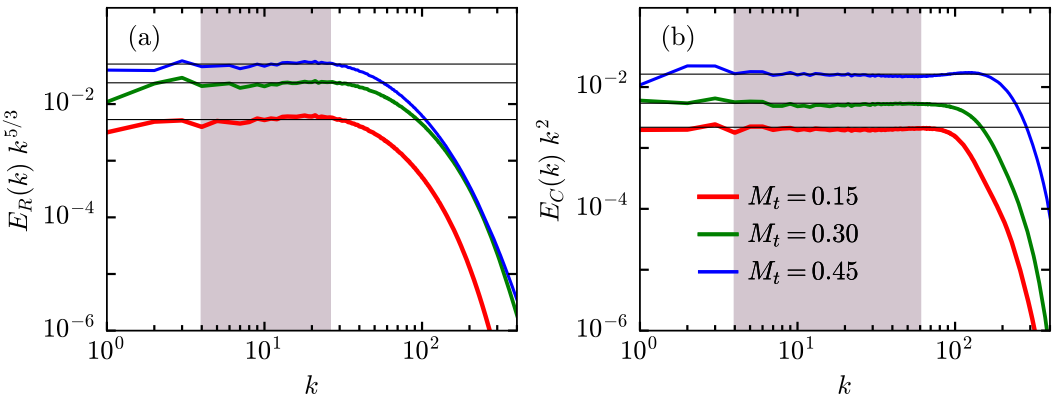

FIG. 2. Compensated energy spectra: (a) rotational kinetic energy, $E_R(k)k^{5/3}$; and (b) compressible kinetic energy, $E_C(k)k^2$, with $M_t = 0.15$ (red), 0.30 (green), and 0.45 (blue). The shaded regions denote the inertial ranges.

[3] H. Tiwari, L. Sharma, and M. K. Verma, Compressible turbulent convection at very high Rayleigh numbers, Int. J. Heat Mass Transf. **242**, 126821 (2025).